

Article

Interlayer Shear Sliding Behaviors during the Fracture Process of Thick Sandstone Roof and Its Mechanism Leading to Coal Mine Tremors

Xuepeng Gao ¹ , Yishan Pan ^{1,2,*}, Tongbin Zhao ³, Wei Wang ¹, Yonghui Xiao ⁴, Yimin Song ⁵ and Lianpeng Dai ²

¹ Key Laboratory of Ministry of Education on Safe Mining of Deep Metal Mines, Northeastern University, Shenyang 110819, China; xuepeng150@163.com (X.G.); wangwei19951996@163.com (W.W.)

² Institute of Disaster Rock Mechanics, Liaoning University, Shenyang 110136, China; DAI_lianpeng1992@163.com

³ School of Energy and Mining Engineering, Shandong University of Science and Technology, Qingdao 266510, China; ztbwh2001@163.com

⁴ School of Physics, Liaoning University, Shenyang 110136, China; yonghui20062009@126.com

⁵ School of Civil Engineering, North China University of Technology, Beijing 100144, China; ssyymmok@sina.com

* Correspondence: panyishan@lnu.edu.cn; Tel.: +86-024-62202013

Abstract: To explore the causes of mine tremors in coal mines with sandstone roofs, a three-point bending loading experiment was designed for composite sandstone layers, and the fracture and interlayer shear slip characteristics of the composite sandstone layers were studied using optical measurement and acoustic emission techniques. The results show that the bending of the rock layers led to interlayer sliding deformation, while the fracturing greatly promoted interlayer sliding. The maximum interlayer slip accelerations during bending deformation and fracturing were 0.6 mm/s^2 and 3.8 mm/s^2 , respectively. During the fracturing of the rock layers, the proportion of acoustic emission shear fracture events increased with the continuous occurrence of long-lasting and high-amplitude acoustic emission events. The mechanism of mine tremors in thick sandstone roofs is as follows: the increase in the area of the goaf causes rock bending deformation and fracturing, accompanied by interlayer shear slip, fracturing of the sandstone layer, and friction dislocation at the cementation surface of the adjacent sandstone layers, which jointly cause vibration of the roof.

Keywords: mining tremors; hard roof; interlayer shear slip; coalburst; fracturing



Citation: Gao, X.; Pan, Y.; Zhao, T.; Wang, W.; Xiao, Y.; Song, Y.; Dai, L. Interlayer Shear Sliding Behaviors during the Fracture Process of Thick Sandstone Roof and Its Mechanism Leading to Coal Mine Tremors. *Appl. Sci.* **2024**, *14*, 4323. <https://doi.org/10.3390/app14104323>

Academic Editor: José Campos Matos

Received: 9 April 2024

Revised: 13 May 2024

Accepted: 16 May 2024

Published: 20 May 2024



Copyright: © 2024 by the authors. Licensee MDPI, Basel, Switzerland. This article is an open access article distributed under the terms and conditions of the Creative Commons Attribution (CC BY) license (<https://creativecommons.org/licenses/by/4.0/>).

1. Introduction

Mining tremors are seismic activity triggered by mining activities [1–3]. There are records of mine tremors in many countries such as Poland, South Africa, Russia, Germany, and the United States [4–6]. For example, a magnitude 3.9 collapse earthquake occurred in Utah, USA on 6 August 2007, which caused six miners to be trapped underground and attracted widespread media coverage [7]. In recent years, the issue of mine tremors has been increasingly recognized in China, and multiple mine tremor events have occurred in provinces such as the Inner Mongolia Autonomous Region, Shaanxi Province, Shandong Province, Liaoning Province, and Jilin Province. The coal mine working face usually includes the coal seam, floor, roof, and roadways on both sides, and the goaf behind will gradually increase with the mining of the coal seam (Figure 1). Based on the subject of energy release, these coal mine tremors can be classified into two types: fault-type tremors, which are caused by the slippage of faults, and roof-type tremors, which are triggered by goaf roof collapse.

In the records of China's coal mine tremors, the fault-type tremor with the highest magnitude was the M_L 4.3 tremor that occurred in the Taiji Coal Mine in Liaoning on 28 April 1977 [8]. The roof-type tremor with the highest magnitude was the M_L 4.2 tremor

that occurred in Shenmu City, Shaanxi Province, on 14 October 2004. In the northern region of Shaanxi Province and the adjacent Ordos region, roof-type tremor events with magnitudes exceeding M_L 2.0 occurred more than 20 times annually [9]. Although there are generally no casualties, these events have caused varying degrees of surface fissuring and house cracks and have even triggered underground coalbursts, leading to concerns among residents about safety in the mining area (Figure 2). This indicates that the prevention and mitigation of mine tremors are of undeniable significance for maintaining the natural ecology of the mining area, ensuring the safety of underground production, and safeguarding the well-being of residents.

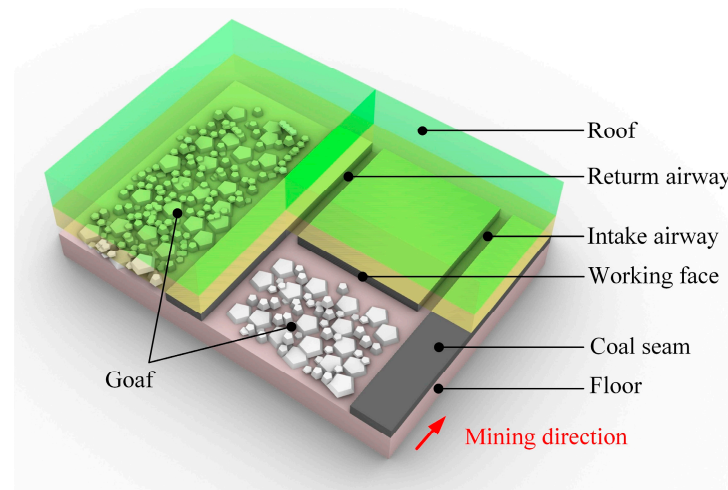


Figure 1. Composition of coal mine working face.

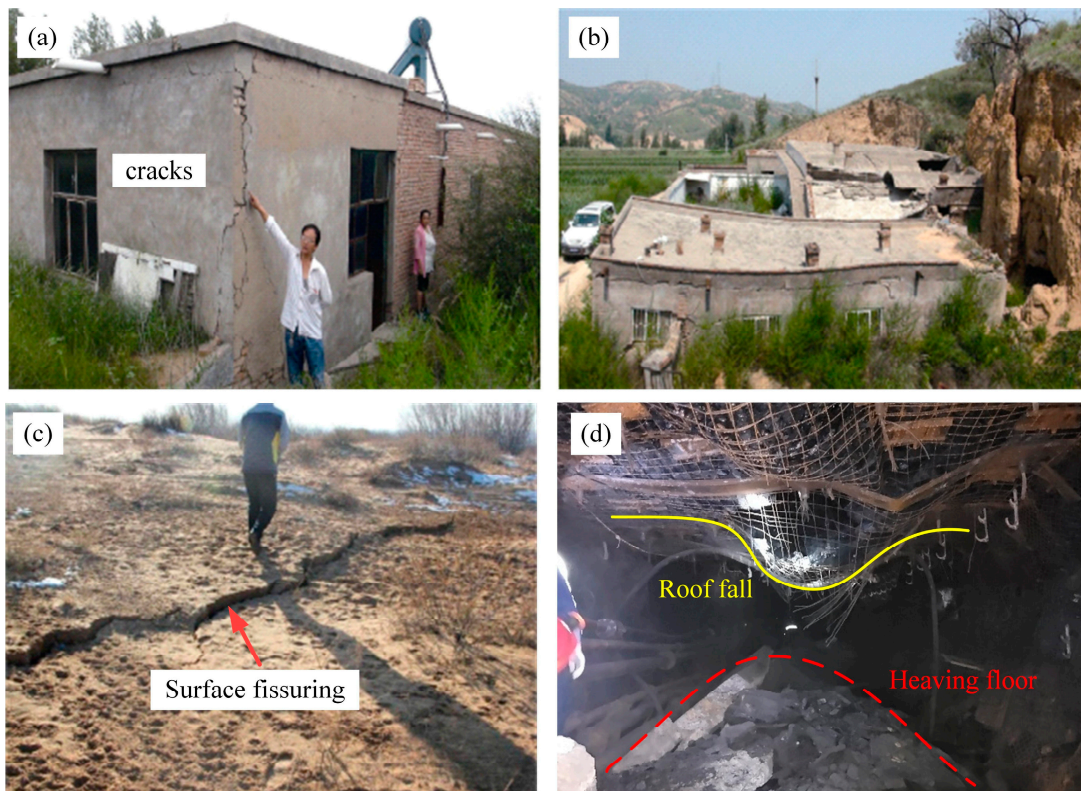


Figure 2. Damage caused by mine tremors on the surface and underground: (a,b) cracking and deformation of buildings [10]; (c) surface fractures; and (d) underground coalburst damage.

The mechanism of mine tremors is a hot topic in the field of rock mechanics. Compared to fault-type tremors, the mechanism of roof-type tremors is less clear. The former has a generation similar to that of natural earthquakes, and their occurrence is accompanied by the shear fracturing of the rock mass and stick-slip motion on faults. This has been confirmed by numerous experiments and field data collected by researchers [11–13]. It is inappropriate to attribute roof-type tremors solely to the fracturing of rock strata. This phenomenon frequently occurs during coal extraction as the rock strata reach their tensile stress limits especially when the rock strata are relatively hard. However, only a very small number of mines experience tremors. Undeniably, the regions where roof-type tremors occur commonly host rigid roofs, and the energy released by the tensile fracturing of these rigid roofs is considerable. This can sometimes lead to dynamic disasters such as coalbursts [14–16]. However, these dynamic disasters occur instantaneously and have a very short duration, contrasting significantly with the sensation felt by surface residents in the tremor areas, which can last for tens of seconds. For instance, on 7 December 2012, a mine tremor occurred in the goaf of the Changxing Coal Mine in Yulin City, Shaanxi Province. Local residents described a sudden loud noise followed by a rumbling sound, accompanied by a sensation of the buildings beginning to sway. The recognition of the sensing of vibrations suggests that the mine tremor waveform had a prolonged duration and low frequency. The research on acoustic emissions associated with rock fracturing indicates that low rise time and high frequency are typical characteristics of tensile-type fractures, while shear-type fractures typically result in longer wave forms, longer rise times, and lower frequencies [17]. Therefore, the cause of roof-type mine tremors is not solely related to the tensile fracturing of hard roofs but is also related to shear fracturing during the process of rock layers fracturing.

In many instances, the hard rock strata above coal seams are typically sandstones formed through sedimentation. Despite variations in their thickness and strength, they occur as layered structures and have interlayered weak structural planes. These interlayer structural planes separate the rock layers and are often argillaceous-cemented inside. They influence the flexural behaviors and fracture patterns of the rock strata, complicating the rupture mechanism of the seismic sources of roof-type tremors. Some mines have exhibited characteristics of synchronous fracturing in multiple layers of thick hard sandstones [18]. The interactions between different sandstone layers merit further study, especially considering the impact of interlayer rupture as it may be a factor contributing to increased shear rupture components at the seismic source.

Fu et al. [19] utilized a borehole tiltmeter to monitor the movement of the overlying strata, and they found that the overlying strata underwent numerous shear movements during the extraction process of the coal seam. The horizontal displacement between different strata increases with depth, suggesting that the overlying strata of the coal seam can generate interlayer slippage, and the interlayer failure must be shear failure. Alneasan et al. [20] investigated the behavior of interfacial cracks between two distinct rock layers under tensile and compressive conditions. Li et al. [21] and Wang et al. [22] examined the influence of bedding interfaces on rock crack trajectories. Zhen et al. [23] found that the interlayer shear friction is governed by the shear strength at the interface, and interlayer sliding can disrupt the integrity of the beam cross-section, leading to a decrease in the flexural strength. Shaban-imashcool et al. [24] pointed out that horizontal stress has an impact on rock layer buckling, crushing, and abutment sliding. Abutment (rock mass that supports the beam at both ends of the beam) sliding may occur in beams with low span–thickness ratios (i.e., thick beams), while crushing and buckling occur in slender beams [25]. Chang et al. [26] experimentally determined that the interface strength significantly influences the propagation of rock fractures, and interfacial debonding occurs when the interface strength falls below a critical threshold. Xiao [27] theoretically analyzed the interlayer shear conditions under bending conditions for layered rock masses and concluded that the interlayer sliding depends on the geometric form of the rock layers, the level of loading, and the interlayer shear strength. The occurrence of earthquakes, water inflow, fires, and other disasters will also lead to

a reduction in the strength and deformation parameters of the layered strata, which is also an important factor affecting the stability design of the goaf [28]. Although researchers have achieved significant research results in terms of the stress distribution, deformation, and fracture characteristics of composite beams, further research is needed to understand the interlayer shear sliding behavior of composite rock masses and its interaction with rock layer fracturing.

In this study, to investigate the fracture and interlayer shear sliding behavior of composite rock layers, a three-point bending experiment was designed for composite sandstone specimens. A quantitative analysis was conducted to study the fracturing, deformation, interlayer sliding acceleration characteristics, and acoustic emission features of the composite rock layers. The aim of this study was to investigate the behavior of interlayer shear sliding that occurs during the bending process of composite rock strata and, subsequently, to discuss the mechanism of roof-type mine tremors. The results of this study provide a reference for the prevention and control of coal mine tremors.

2. Experimental Methods

2.1. Specimen Processing and Sensor Placement

The experimental design takes into account the geological conditions of thick sandstone layers in the Ordos region of China. During coal mining in these areas, there are often thick sandstone layers above the coal seam. The sample also selected sandstone with similar rock strength to this area (strength of about 60 MPa). The size and proportion of the sample were also treated according to the possible size of the thick sandstone roof above the coal mine working face in the Ordos region, and the scale was set to 1:1000 mm. The corresponding real geological situation is as follows: the span of the goaf is 300 m, and the thickness of the sandstone layer is 100 m. The flatness of rock samples is referenced against “regulation for testing the physical and mechanical properties of rock—Part 22: Test for determining the flexural strength of rock”. Therefore, we prepared two rectangular ($350 \times 50 \times 50$ mm) sandstone specimens. After applying an even layer of black matte primer to one face of these specimens, we sprayed white speckle patterns on them using white matte paint (Figure 3a). The two rock specimens stacked together were considered to be a composite rock layer specimen. A rectangular specimen with dimensions of $350 \times 100 \times 50$ mm was prepared as a counterpart for comparison.

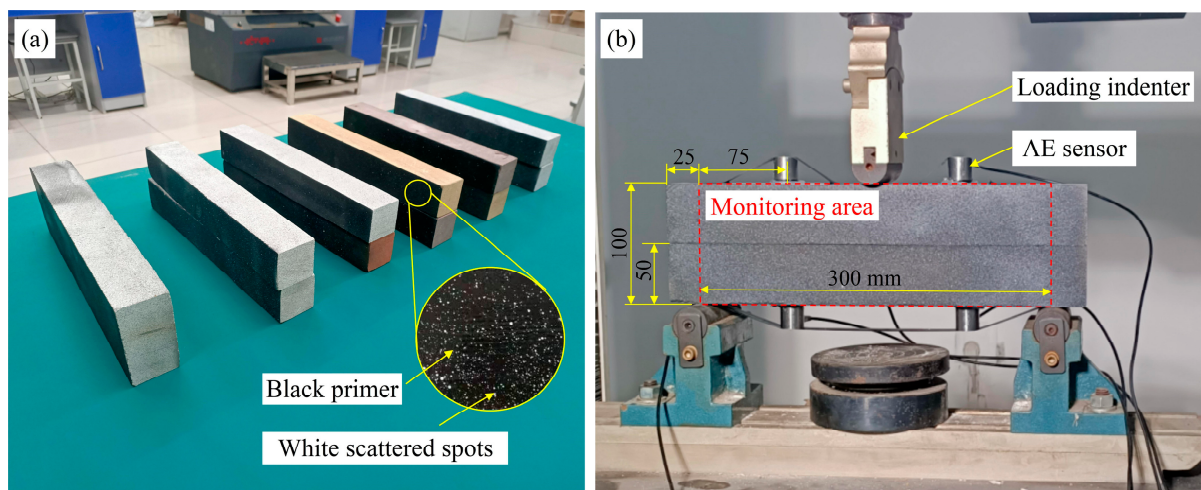


Figure 3. Experimental preparation: (a) partially prepared rock specimens; and (b) arrangement of sensors.

The prepared specimens were placed on the support bases of a three-point bending test apparatus (Figure 3b). The left and right support bases were both located 25 mm away from the specimen's lateral edges, and the remaining 300 mm length served as the region

for speckle monitoring. Two acoustic emission sensors were installed on each of the upper and lower surfaces of the composite rock specimen, and one sensor was installed at the central position at the rear of the specimen.

2.2. Experimental System

The experiment was conducted at Shandong University of Science and Technology. The experimental system comprised a loading system and a monitoring system. The loading system, a Kexin Wow3100 universal testing machine (Kexin, Shenzhen, China), employed a three-point bending test method to apply a load to the specimens depicted in Figure 3. The loading was controlled through displacement, with a loading rate of 0.001 mm/s. The monitoring system was constituted of an optical measurement monitoring system and an acoustic emission monitoring system. The optical measurement monitoring system utilized a high-speed industrial camera to capture surface images throughout the entire loading process of the specimen, with an image data acquisition rate of 5 frames per second. The acoustic emission monitoring system was an AMSY-6 acoustic emission signal analyzer produced by the German company Vallen (Wolfratshausen, Germany), which collected acoustic emission information from the sensor (Figure 3b). The system was set with a preamplifier gain of 40 dB, a threshold of 10 mV, and a sampling frequency of 3 MHz. Figure 4 presents a schematic diagram of the experimental system.

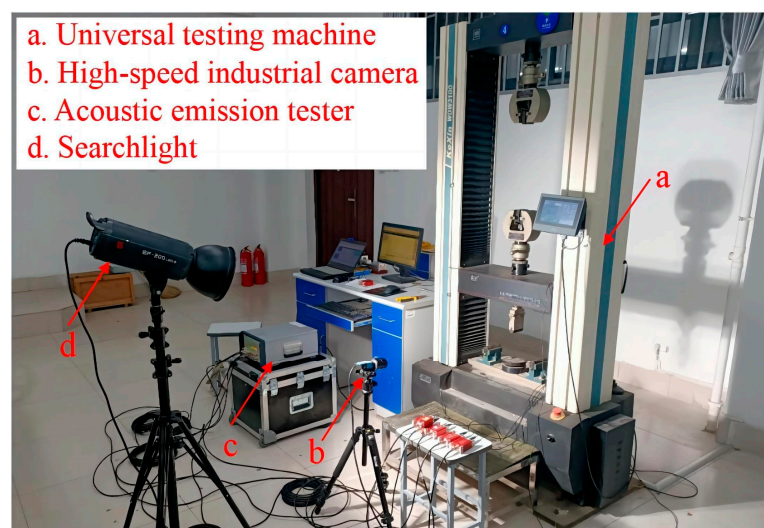


Figure 4. Composition of the experimental system.

2.3. Experimental Procedure

First, the prepared specimen was placed on a three-point bending test apparatus; its position was adjusted to ensure that the loading indenter was centered on the upper surface of the specimens. Black insulating tape was used to install the acoustic emission sensors at designated locations on the surface of the specimen, and white Vaseline was applied between the specimen and the sensors to enhance the coupling effect. The position, angle, and intensity of the searchlight source were then adjusted to ensure uniform brightness on the side of the specimen where the sprayed speckles were located. A high-speed camera was fixed about 1.2 m from the specimen, and the camera's angle, aperture, and resolution were adjusted to achieve the sharpest image. Time calibration was then performed on the loading system, optical measurement monitoring system, and acoustic emission monitoring system to ensure that their recorded times remained consistent throughout the experiment. At the start of the experiment, displacement-controlled loading was applied, and the loading system collected the load–time curve. The high-speed industrial camera recorded the speckle images on the surface of the specimens, and the acoustic emission monitoring system collected the acoustic emission signals generated during the experiment until the

specimen was completely destroyed. After the experiment was completed, the relevant experimental data were analyzed and processed.

3. Experimental Results

3.1. Fracture Characteristics of Composite Rock Layer under Bending Loading

Figure 5 presents the load–displacement curves and fracture patterns of the composite rock layer specimens. For comparison, the loading curve of an intact specimen is included in Figure 5a. During the loading phase of the test, the load on the composite rock layer specimen gradually increased to a peak load of 7.77 kN. Initially, microcracks appeared in the upper portion of the rock specimen, and, then, the load suddenly decreased to 4.11 kN. Subsequently, the load briefly increased to 4.20 kN before both the upper and lower portions of the rock fractured, leading to the complete loss of the load-bearing capacity of the specimen. In contrast, the intact specimen exhibited a greater secant modulus and a higher peak load before reaching its peak, which were 1.63 and 1.93 times that of the composite rock layer specimen, respectively. The integral of the curve yielded an elastic strain energy of 2.93 J for the composite rock layer specimen, and the energy for the intact specimen was 4.12 J.

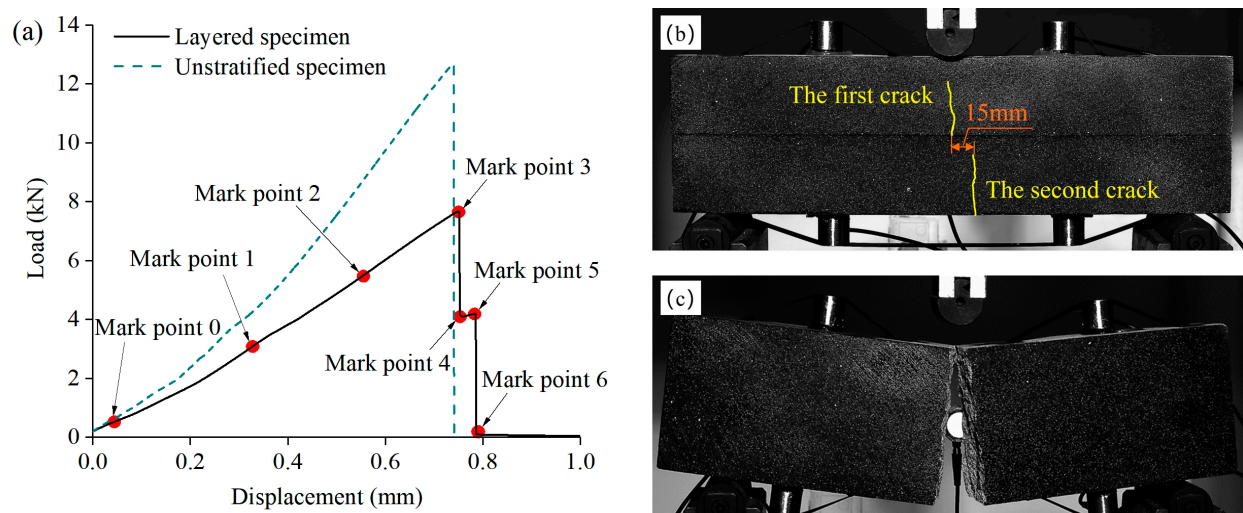


Figure 5. Fracture characteristics of two specimens: (a) load–displacement curves; and (b,c) fracture locations.

The fracture in the upper layer of the composite rock layer specimen was located close to the center of the specimen, whereas that in the lower layer was not. The fracture in the lower layer was located 15 mm from that in the upper layer. In contrast, the fracture in the intact rock specimen was located at the center of the specimen. Therefore, for roof rocks of equal thickness, the presence of a layering interface significantly reduces its load-bearing capacity and shifts the location of the fracture in the lower layer, leading to a non-pure bending deformation.

3.2. Evolutionary Law of Composite Rock Layer Deformation

3.2.1. Vertical Deformation

To analyze the deformation evolution of the rock specimens during loading, seven marker points (points 0–6) were selected (Figure 5). The vertical displacement of the specimen at the different points is shown in Figure 6. The contact surface between the two layers of rock was located at $y = 50$ mm. When the specimen was loaded to the positions of points 1–3, the vertical deformation of the upper layer of the rock was generally greater than that of the lower layer of the rock, and the deformation gradually exhibited a bilaterally symmetric distribution. Locally at both ends of the specimen, the isoclines of

the deformation exhibited a step-like change along the contact surface, while the isoclines in other areas were smoother. When the loading reached the position of point 4, the upper layer of rock was the first that underwent fracturing, with a limited flexural deformation before the development of a 0.54 mm-long fracture. At the interface in the left half of the rock specimen, the isoclines of the vertical deformation exhibited a stepped change, indicating that the left half of the upper layer of the rock underwent an abrupt horizontal dislocation upon fracturing. After the upper layer of rock fractured, the load-bearing body transitioned to the lower layer of the rock. The vertical deformation of the lower layer of the rock continued to increase. The maximum deformation was located about 15 mm to the right of the center position and caused fracturing.

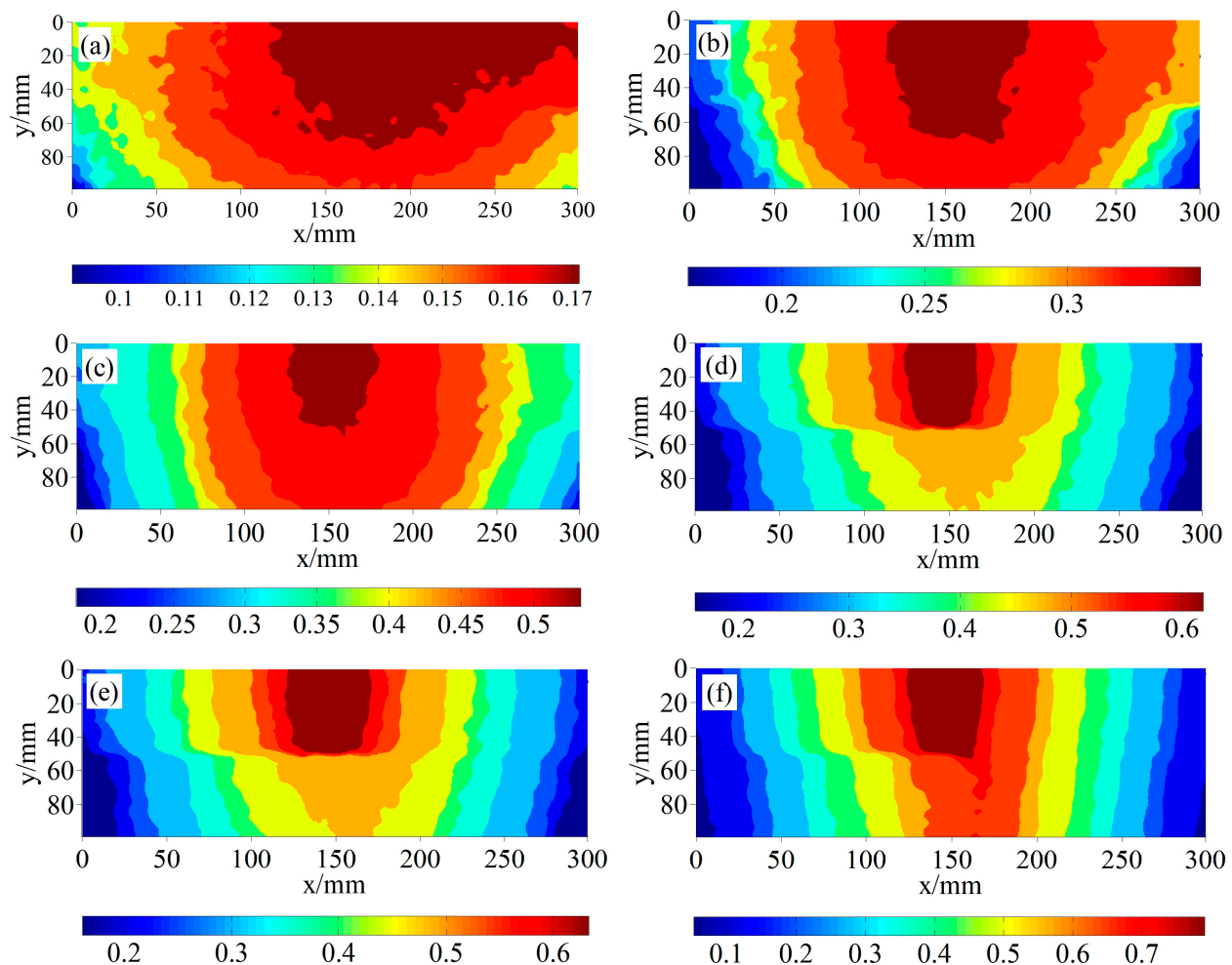


Figure 6. Vertical displacements of composite rock layer specimens at (a) Point 1; (b) Point 2; (c) Point 3; (d) Point 4; (e) Point 5; and (f) Point 6.

3.2.2. Horizontal Deformation

The horizontal displacement of the specimen at points 1–3 is shown in Figure 7. Compared to the vertical displacement, the impact of the interface on the horizontal displacement of the specimen was more pronounced. As can be seen from Figure 6a–c, the horizontal deformation of the rock was discontinuous on both sides of the interface during the loading process, and the deformation difference between the upper and lower layers of the rock near the ends of the rock increased, reaching a maximum of 0.13 mm. This indicates that there was a horizontal movement between the upper and lower layers of the rock specimen during the loading process. When the loading reached point 4, the upper layer of the rock fractured, and the parts of the rock on either side of the fracture

moved in opposite directions. The interlayer displacements at the left and right ends of the specimen were 0.14 and 0.2 mm, respectively; i.e., we recorded increases of 0.1 and 0.07 mm compared to point 3. This process was transient. When the loading exceeded point 5, the interlayer displacements at the left and right ends of the specimen were 0.09 and 0.35 mm, i.e., increases of -0.08 and 0.14 mm compared to point 4, and the fracturing of the lower layer of the rock promoted the transient interlayer displacement.

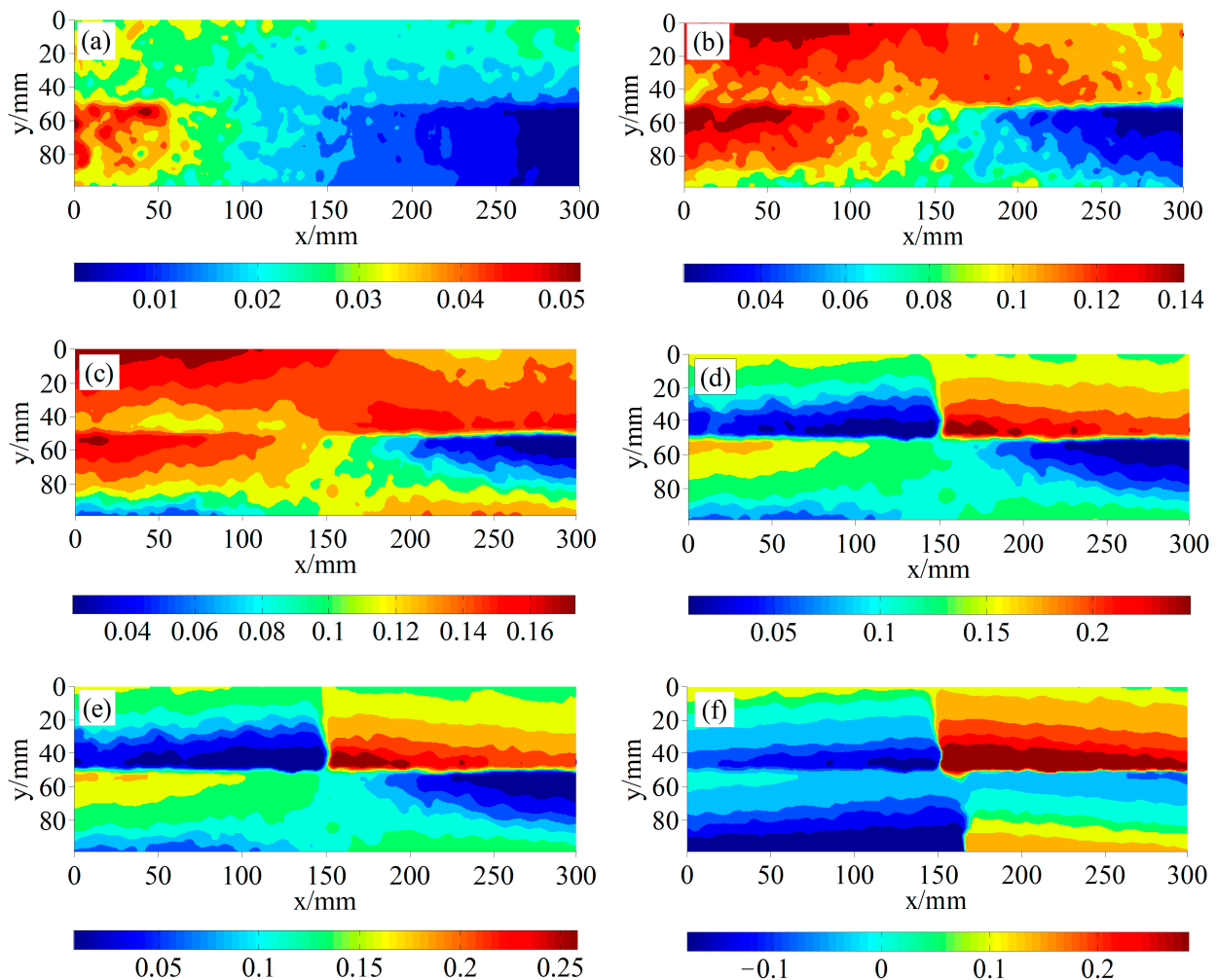


Figure 7. Horizontal displacements of composite rock layer specimens at (a) Point 1; (b) Point 2; (c) Point 3; (d) Point 4; (e) Point 5; and (f) Point 6.

3.2.3. Shear Deformation

Figure 8 depicts the shear deformation evolution at points 1–6. Upon loading to points 1, 2, and 3, there were distinct deformation zones at the delamination interfaces, and these zones extended from both ends toward the middle. At point 3, the maximum shear strain was 0.015. Upon loading to point 4, the maximum shear deformation increased to 0.025, i.e., an increase of 0.01 compared to point 3. Moreover, the fracturing of the upper layer of the rock caused a sudden increase in the interlayer shear strain, which caused the deformation zone at the interface to extend throughout the specimen. Upon loading to point 6, the maximum shear deformation increased to 0.047, i.e., with an increase of 0.02 compared to point 5. The fracturing of the lower layer of the rock again promoted a transient increase in the interlayer shear deformation.

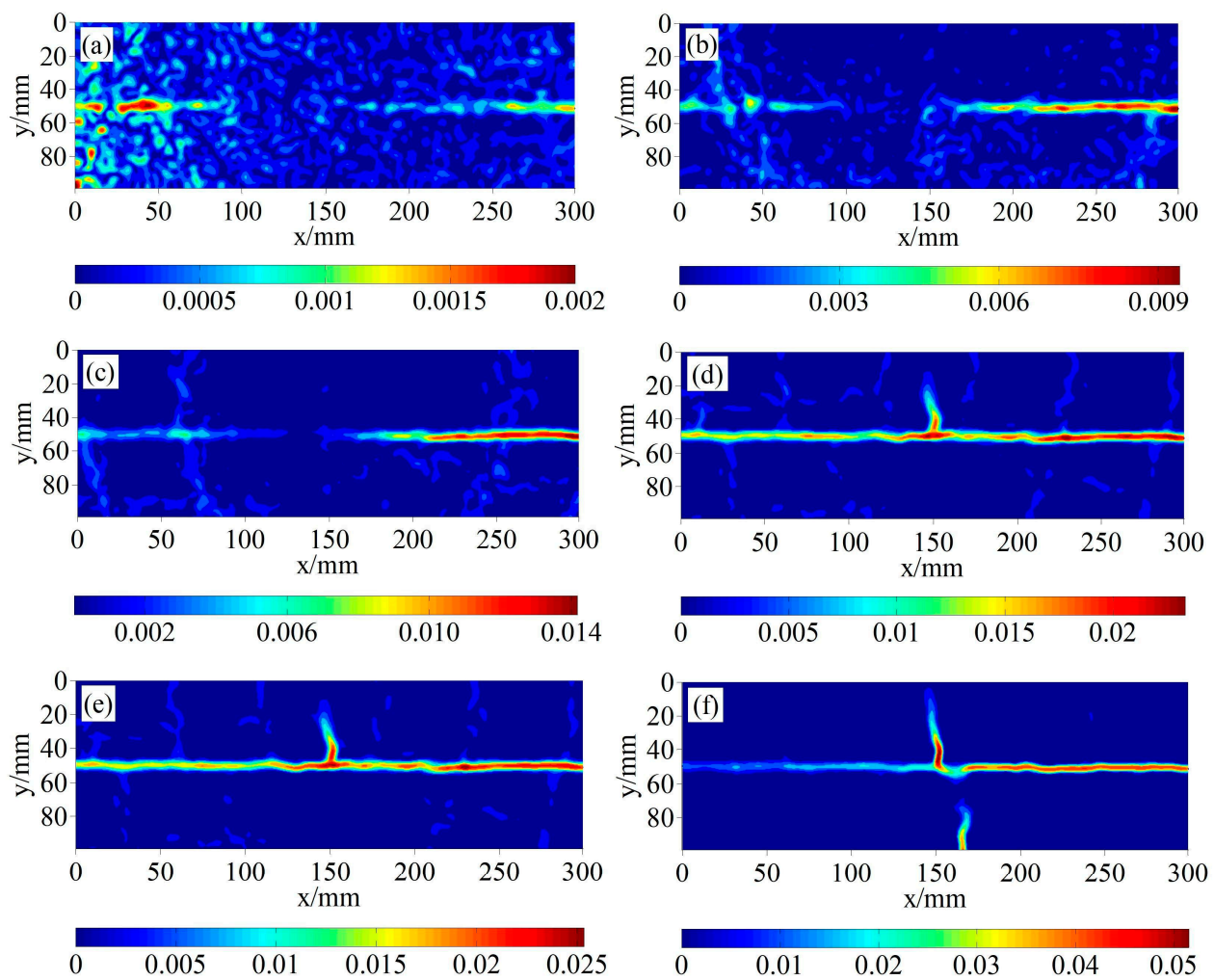


Figure 8. Shear strains of composite rock layer specimens at (a) Point 1; (b) Point 2; (c) Point 3; (d) Point 4; (e) Point 5; and (f) Point 6.

3.3. Characteristics of Interlayer Sliding Acceleration

To further observe the acceleration characteristics of the interlayer sliding, two 5×5 pixel square windows were selected approximately 25 mm above and below the interface in the middle and on the left and right ends of the speckle observation area. The connection line between the two square windows was perpendicular to the interface of the specimen. By calculating the x-co-ordinates of the center points of the two square windows in each image and their difference, we analyzed the characteristics of the interlayer sliding displacement and acceleration change during loading. The time interval between each image was approximately 0.2 s. The arrangement of the measuring points and the change in the interlayer sliding displacement are shown in Figure 8a. When the load reached approximately 20% of the peak value, the interlayer sliding displacement at measuring points 1–3 began to change significantly, and the interlayer sliding displacements at the different measuring points did not vary synchronously. The maximum interlayer sliding displacement during the rock bending deformation was 0.046 mm and was located at measuring point 3. The rock fracturing caused a sudden increase in the interlayer sliding displacement, with instantaneous increases of 0.051, 0.156, and 0.081 mm at measuring points 1, 2, and 3, respectively. Among them, the interlayer sliding displacement at measuring point 1 exhibited a negative growth trend during the rock fracturing, followed by a positive growth trend. This was caused by the inconsistent directions of the interlayer sliding caused by the rock fracturing at measuring point 1 and by the bending deformation.

The change in the interlayer slip acceleration (Figure 9b) exhibited intermittent characteristics during the bending deformation stage, with a maximum interlayer slip acceleration of 0.6 mm/s^2 at measuring point 2. During the rock fracture deformation stage, it exhibited a sudden increase, and the slip increased earlier at both ends of the rock than in the middle of the specimen, with a maximum interlayer slip acceleration of 3.8 mm/s^2 at measuring point 2. Therefore, the rock bending led to an interlayer slip deformation, while the rock fracturing greatly promoted the interlayer slip.

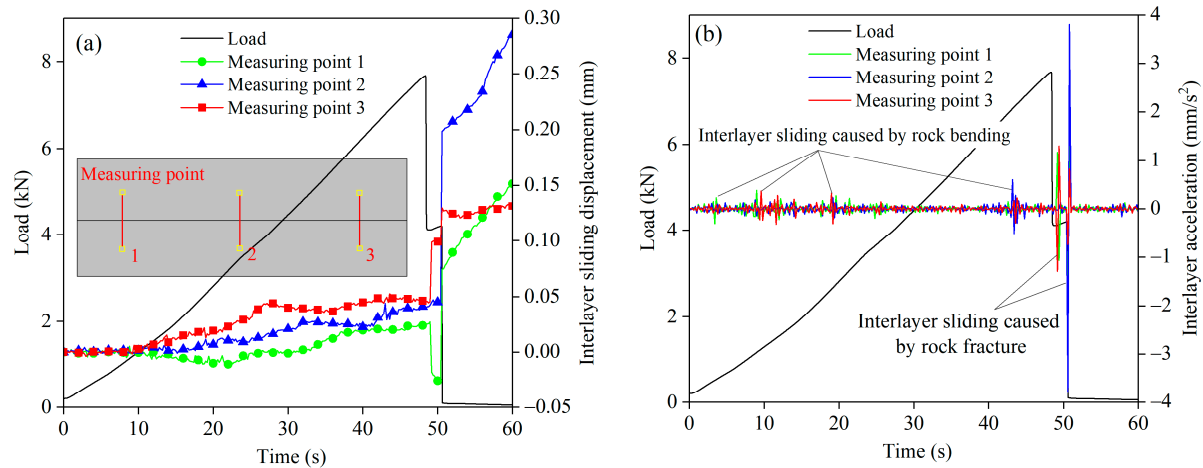


Figure 9. Variation characteristics of interlayer slip: (a) interlayer slip displacement; and (b) interlayer slip acceleration.

3.4. Acoustic Emission Characteristics

3.4.1. Acoustic Emission Count and Energy

The acoustic emission ringing count and cumulative energy statistics during the loading process are shown in Figure 10. Before the fracturing of the specimen, the acoustic emission ringing count gradually increased with increasing load; however, from the perspective of the change in the energy, the energy of the early acoustic emission specimen was very small. When the specimen approached the occurrence of fracturing, the acoustic emission ringing count significantly increased, and the maximum value occurred before the peak load. Based on the analysis of the evolution of the interlayer deformation field, this was the result of the combined effects of the interlayer sliding and rock fracture expansion.

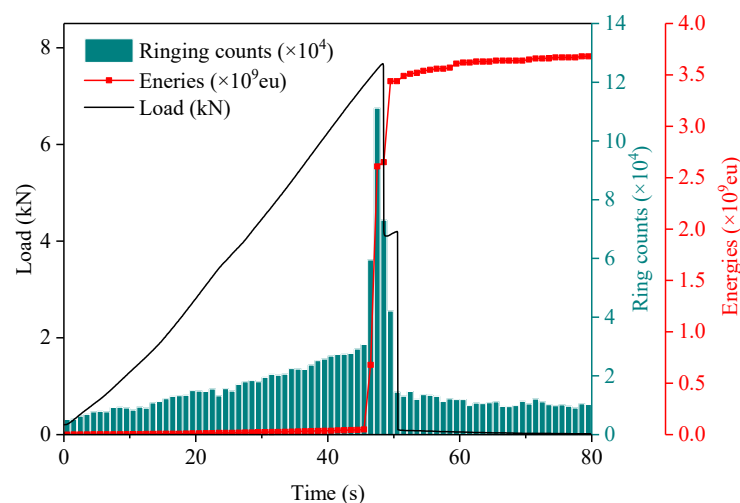


Figure 10. Statistics of the acoustic emission events of the rock specimens.

3.4.2. Damage and Crack Evolution

Among the acoustic emission parameters, two waveform parameters, the rising angle (RA) and average frequency (AF), can be used to determine the type of crack [29]. The RA value is equal to the ratio of the rise time to the maximum amplitude, and the AF value is equal to the ratio of the ringing count (number of times the acoustic emission signal exceeds the detection threshold) to the duration. Tension cracks are characterized by a low rise time and high frequency, while shear cracks usually result in longer waveforms, as well as longer rise times and lower frequencies [30]. The RA-AF distribution of the acoustic emission events in the composite rock layer of the specimen is shown in Figure 11a, in which the data points in the central region are magnified. It can be seen that both tension cracks and shear cracks formed during the loading process of the sample, and the proportion of the tension cracks was higher than that of the shear cracks.

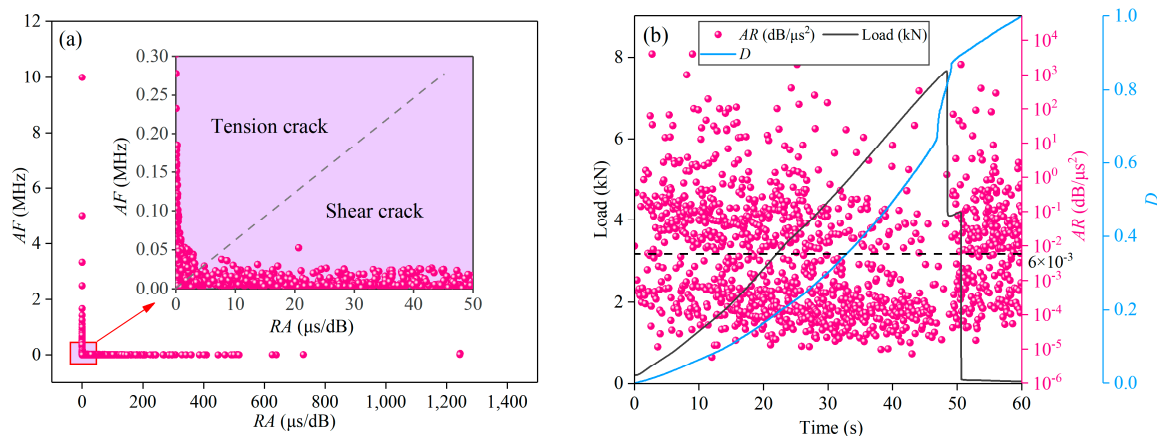


Figure 11. Crack and damage evolution of acoustic emission: (a) crack classification; and (b) variations in the D and AR values with the loading level.

To obtain the time-varying characteristics of the microcrack development during the different loading stages, the AR value was defined as $AR = AF/RA$. A larger AR value denotes tension cracks and a smaller AR value denotes shear cracks. In addition, the damage variable D is defined as follows:

$$D = \frac{\sum_0^t N_t}{\sum_0^T N_t}, \quad (1)$$

where N_t is the number of rings at the current time, t is the time, and T is the total experimental time.

The evolution of the cracks and damage in the specimen at different loading times is shown in Figure 11b. The tension cracks mainly clustered in the AR value range of 0.006 – $1.2 \text{ dB}/\mu\text{s}^2$, while the shear cracks mainly clustered in the AR value range of 1×10^{-5} – $0.001 \text{ dB}/\mu\text{s}^2$. The damage to the rock specimen generally occurred in three stages, namely, the nonlinear increase stage (0 – 46.7 s), the accelerated increase stage (46.7 – 49.1 s), and the stable increase stage (49.1 – 60 s), which corresponded to the bending, fracturing, and post-peak deformation stages of the rock, respectively. In the bending deformation stage of the rock, both the shear cracks and tension cracks propagated, and, before the specimen fractured, the proportion of shear cracks gradually increased, indicating that the degree of shear dislocation between the layers continued to increase. In the fracture deformation stage of the rock, the AR value of the acoustic emission events was low, and the proportion of shear fractures was higher than that of the tensile fractures, which was opposite to the situation when the tensile fractures dominated in a single-layer rock.

3.4.3. Acoustic Emission Duration

Based on the evolution of the interlayer deformation of the test specimen, it was found that the fracturing of the specimen was accompanied by an interlayer shear dislocation. The existence of interlayer shear fractures caused the rock stratum to develop a mixed tensile–shear fracture during fracture, rather than pure tensile fractures. The increase in the shear fracture components led to longer waveforms and lower frequencies. Figure 12 shows that continuous acoustic emission events with long durations and high amplitudes occurred during the fracturing of the specimen, which made the waveform generated by the fracture longer. This made the fracture waveform longer during the rock fracturing, and the duration of the vibration increased, which explains to some extent why the duration of roof-type mine tremors can reach several seconds.

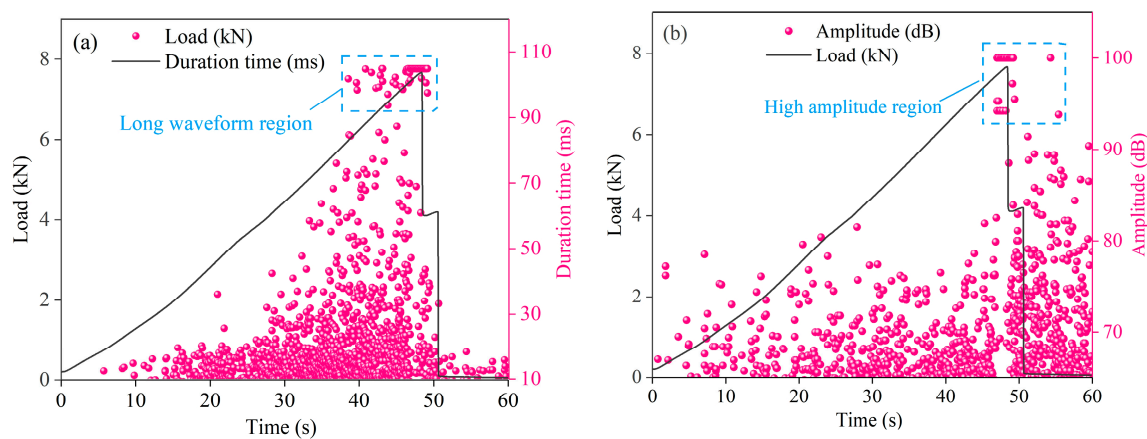


Figure 12. Relationships between the loading curve and the (a) acoustic emission duration and (b) amplitude.

4. Conditions of Interlayer Shear Slip in Composite Rock Layers and the Possible Mechanism of Mine Tremor

4.1. Interlayer Slip Conditions of Composite Rock Layers

The experiment was simplified to a composite, simply supported beam model with a concentrated force P acting on the top (Figure 13). The dimensions and material properties of beam 1 and beam 2 were exactly the same. Compared with other analogic models, this model is a basic mechanical model of rock beams. The focus of the model is when the interlayer shear slip occurs rather than when the rock beams will fracture.

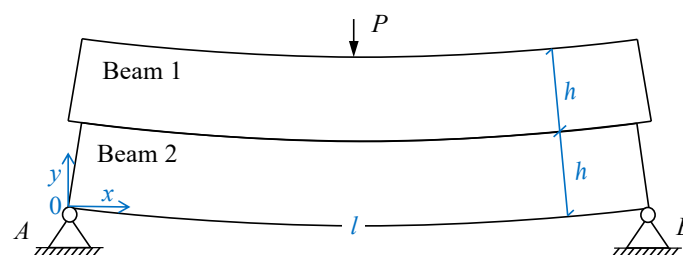


Figure 13. Simple beam model of composite sandstone layers.

To simplify the analysis, it was assumed that the interface was exactly located at the neutral axis of the composite, simply supported beam. According to the theory of material mechanics, a constant shear stress τ will be generated between the layers:

$$\tau = \frac{3P}{2bh\left(1 + \sqrt{\frac{E_t}{E_c}}\right)}, \quad (2)$$

where h is the thickness of the beam; b is the width of the beam section; E_t is the Young's modulus; and E_c is the bulk modulus.

When τ is greater than the shear strength between the layers, the combined rock layer will experience interlayer shear sliding during bending. If the friction between the upper and lower layers of the rock is defined as the shear strength between layers, then, in addition to τ , the interlayer shear sliding is also related to the contact force $q(x)$ between the layers and the friction coefficient μ . The starting condition for interlayer shear sliding is

$$\tau \geq \frac{\mu}{b}q(x) + S_{coh}, \quad (3)$$

where μ is the friction coefficient; $q(x)$ is the contact force between the layers; and S_{coh} is the cohesion force of the interface.

The interlayer contact force $q(x)$ is related to the bending stiffness of beams 1 and 2. Under the experimental conditions, the effect of the self-weight of the rock specimen on the deformation of the specimen was neglected, and the mechanical parameters of beams 1 and 2 were the same. The composite beam model shown in Figure 12 was decomposed into two independent, simply supported beam models (Figure 14).

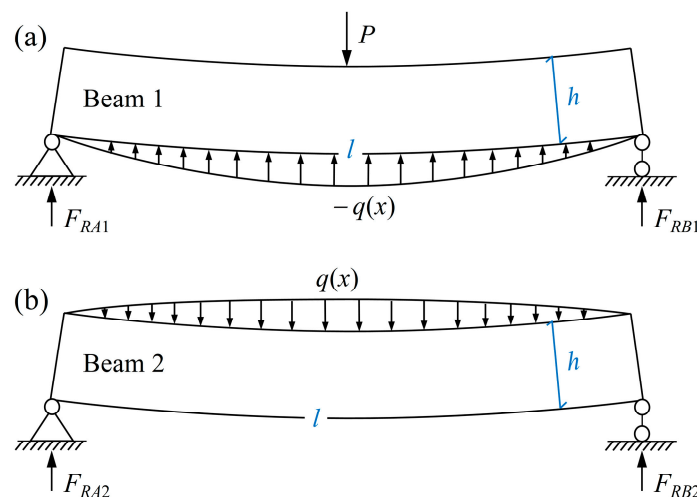


Figure 14. Decomposed model of (a) beam 1 and (b) beam 2.

Considering the symmetry of the beam, the study range was only selected as $0 \leq x \leq l/2$. The deflection curves of beam 1 and beam 2 under independent conditions are

$$w_1(x) = \frac{P}{48E_t I} (4x^3 - 3l^2x) \quad (0 \leq x \leq \frac{l}{2}), \quad (4)$$

$$w_2(x) = 0 \quad (0 \leq x \leq \frac{l}{2}), \quad (5)$$

where I is the moment of inertia of the beam, $I = bh^3/12$.

Assuming that $q(x)$ is proportional to the deflection difference $w_1(x) - w_2(x)$ between beams 1 and 2, then the interlayer contact force function $q(x)$ is

$$q(x) = kb[w_1(x) - w_2(x)] = k \frac{P}{48E_t I} (4x^3 - 3l^2x) \quad (0 \leq x \leq \frac{l}{2}), \quad (6)$$

where k is an undetermined coefficient.

The support reaction forces of beam 1 and 2 are F_{RA1} and F_{RA2} .

$$F_{RA1} = \frac{P}{2} + \int_0^{\frac{l}{2}} -q(x)dx = \frac{P}{2} + \frac{5kPl^4}{768E_t I}, \quad (7)$$

$$F_{RA2} = \int_0^{\frac{l}{2}} q(x) dx = -\frac{5kPl^4}{768E_tI}. \quad (8)$$

The bending moments, $M_1(x)$ and $M_2(x)$, of beams 1 and 2 on any section are

$$M_1(x) = F_{RA1}x + \int_0^x q(x_0)(x - x_0)dx_0 = \frac{P}{2}x + \frac{kP}{48E_tI}\left(\frac{x^5}{5} - \frac{l^2x^3}{2} + \frac{5l^4x}{16}\right), \quad (9)$$

$$M_2(x) = F_{RA2}x - \int_0^x q(x_0)(x - x_0)dx_0 = -\frac{kP}{48E_tI}\left(\frac{x^5}{5} - \frac{l^2x^3}{2} + \frac{5l^4x}{16}\right). \quad (10)$$

According to the principle of virtual work, when a unit load acts on the mid-span of a simply supported beam, the bending moment of the beam is

$$\hat{M}(x) = \frac{x}{2}(0 \leq x \leq \frac{l}{2}). \quad (11)$$

The deflections of beam 1 and beam 2 in the mid-span are

$$W_1 = \frac{2}{E_tI} \int_0^{\frac{l}{2}} M_1(x) \hat{M}(x) dx = \frac{1}{E_tI} \left(\frac{Pl^3}{48} + \frac{kP}{48E_tI} \cdot \frac{67l^7}{13440} \right), \quad (12)$$

$$W_2 = \frac{2}{E_tI} \int_0^{\frac{l}{2}} M_2(x) \hat{M}(x) dx = \frac{1}{E_tI} \cdot \frac{kP}{48E_tI} \cdot \frac{67l^7}{13440}. \quad (13)$$

According to the deformation compatibility condition, the deflections of beams 1 and 2 at the mid-span location of $x = l/2$ are the same, that is, $w_1 = w_2$. This equality can be used to obtain the elastic coefficient k of the interlayer contact force and the contact force function $q(x)$ as follows:

$$k = -\frac{6720E_tI}{67l^4}, \quad (14)$$

$$q(x) = \frac{140P}{67l^4}(3l^2x - 4x^3) \quad (0 \leq x \leq \frac{l}{2}). \quad (15)$$

For the three-point bending test conducted, $P = 5$ kN, $l = 0.3$ m, $b = 0.05$ m, $h_2 = 0.05$ m, $E_t/E_c = 0.5$, $\mu = 0.5$, and $S_{coh} = 0$ MPa were taken and substituted into Equations (2), (3), (14) and (15) to obtain the interlayer shear stress τ and the frictional force provided by the interlayer contact force $\mu/b \cdot q(x)$ (Figure 15a). Therefore, during the loading process, the frictional force provided by the interlayer contact force was less than the interlayer shear stress and shear slip could occur between the layers. The amount of slip was equal to the difference in the elongation between beams 1 and 2. For the actual strata, there is often a bond strength between the layers. When considering the bond strength, it may be convenient to assume $S_{coh} = 1.5$ MPa, at which point the rock formation contains both regions of shear slip and regions without shear slip, and the length of the slip region is x_1 .

If the concentrated load P is replaced by a uniformly distributed load q_0 with an action interval of $[0, l]$, the interlayer shear stress τ and the interlayer contact force function $q(x)$ can be obtained using the same method.

$$\tau = \frac{3q_0(l - 2x)}{4bh_2(1 + \sqrt{\frac{E_t}{E_c}})}, \quad (16)$$

$$q(x) = \frac{336q_0}{l^4}(x^4 - 2lx^3 + l^2x^2) \quad (0 \leq x \leq \frac{l}{2}). \quad (17)$$

For the case of a uniformly distributed load, values of $q_0 = 50$ kN/m, $l = 0.3$ m, $b = 0.05$ m, $h_2 = 0.05$ m, $E_t/E_c = 0.5$, $\mu = 0.5$, and $S_{coh} = 1.5$ MPa are substituted into Equations (2), (16) and (17). The results of the interlayer shear stress and shear strength are shown in Figure 15b. The interlayer shear stress $\tau(x)$ is a linearly decreasing function, and the shear stress increases as it approaches the end of the rock layer. The contact friction

between the layers is a monotonically increasing function, and the interlayer contact force near the end of the rock layer is significantly smaller than that in the middle of the rock layer. In both cases, when there is an interlayer bond strength and it is not considered, the shear strength curve intersects with the shear stress function at $x_1 = 0.12l$ and $x_2 = 0.07l$, respectively. Therefore, before the rock layers fracture, only a small proportion of the fractures near the end can undergo interlayer shear slip, and the proportion in the middle will not undergo interlayer shear slip.

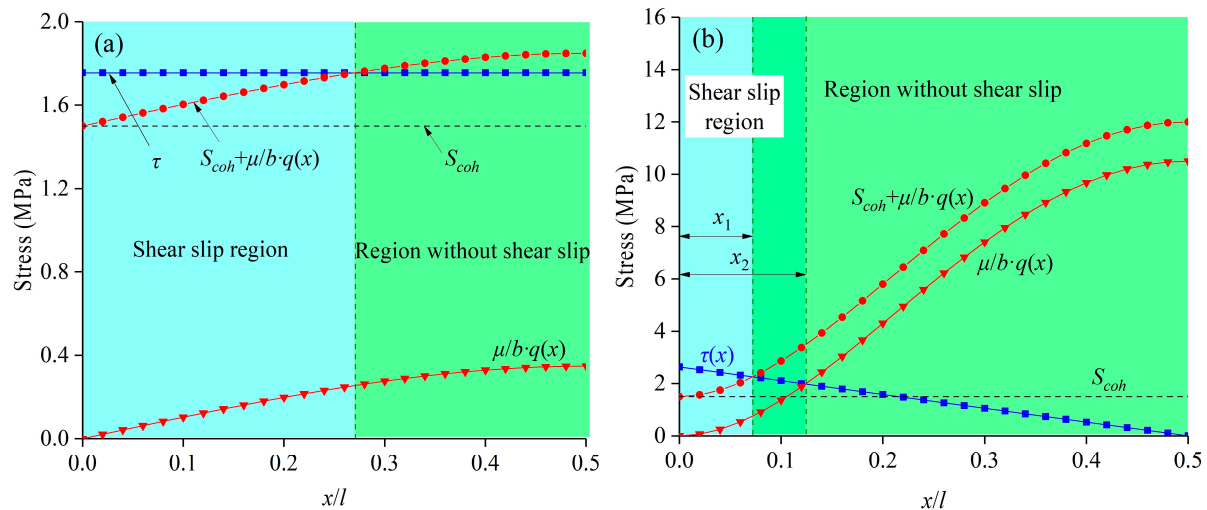


Figure 15. Distributions of shear stress and friction force between the rock layers: (a) under a concentrated load P ; and (b) under a uniformly distributed load q_0 .

4.2. Fracture Sequence of Composite Rock Layers

The interlayer shear slip has a significant impact on the fracturing of the rock strata, and it weakens the integrity of the rock strata. The bending section coefficient of the rock strata that is undergoing interlayer shear slip decreases from $W_t = 2/3bh^2$ to $W_t = 1/6bh^2$, making it more prone to fracturing. According to the maximum tensile stress strength criterion, the fracturing of composite rock layers depends on whether the internal tensile stress reaches a limit value. At the point of fracturing, the rock stratum undergoes extreme bending deformation, and the extreme curvature of the upper and lower layers of rock strata are

$$\frac{1}{\rho_{cr1}} = \frac{2[\sigma_{t1}]}{E_{t1}h_1} \text{ and } \frac{1}{\rho_{cr2}} = \frac{2[\sigma_{t2}]}{E_{t2}h_2} \quad (18)$$

where ρ_{cr1} and ρ_{cr2} are the limiting curvature radii of the upper and lower rock masses (m); $[\sigma_{t1}]$ and $[\sigma_{t2}]$ are the ultimate tensile strengths of the upper and lower rock strata (MPa); and E_{t1} and E_{t2} are the tensile elastic moduli of the upper and lower rock strata (GPa).

As can be seen from Equation (18), the ultimate curvature of a rock stratum is related to its ultimate tensile strength, tensile elastic modulus, and thickness. When bending occurs, if the ultimate curvature of the upper rock stratum is greater than that of the lower rock stratum, the lower rock stratum reaches the ultimate tensile stress first and fractures. If the ultimate curvature of the upper rock stratum is less than that of the lower rock stratum, the upper rock stratum fractures first. If the ultimate curvatures of the two rock strata are the same, there is a high probability that the two rock strata will fracture synchronously. In fact, the fracturing of the upper or lower rock stratum will produce a dynamic load and may even cause the other layer of the rock strata to fracture. In particular, in the case in which the thickness and strength of the two rock strata are relatively close and the upper rock stratum fractures first, the load borne by the lower rock stratum will increase sharply in an instant. For some mining tremor events, underground workers and surface residents have described the sound characteristics as two short-interval muffled explosions followed by a continuous rumbling sound.

4.3. Mechanism of Mine Tremors in Composite Rock Layers

In the sedimentary environment of coal seams, the overlying rock strata are layered. In some mining areas where mining tremors occur frequently, it has been reported that multiple layers of hard sandstone with large thicknesses continuously occur in the strata. They have a large ability to sustain the roof, providing, however, a prerequisite for the occurrence of roof-type tremors. As the size of the goaf increases, they are in a suspended state and undergo bending and subsidence deformation (Figure 16a). The interface undergoes shear sliding because of poor cohesion (Figure 16b), which is accompanied by an energy release. However, due to the small amount of sliding, the magnitude of the energy is not large.

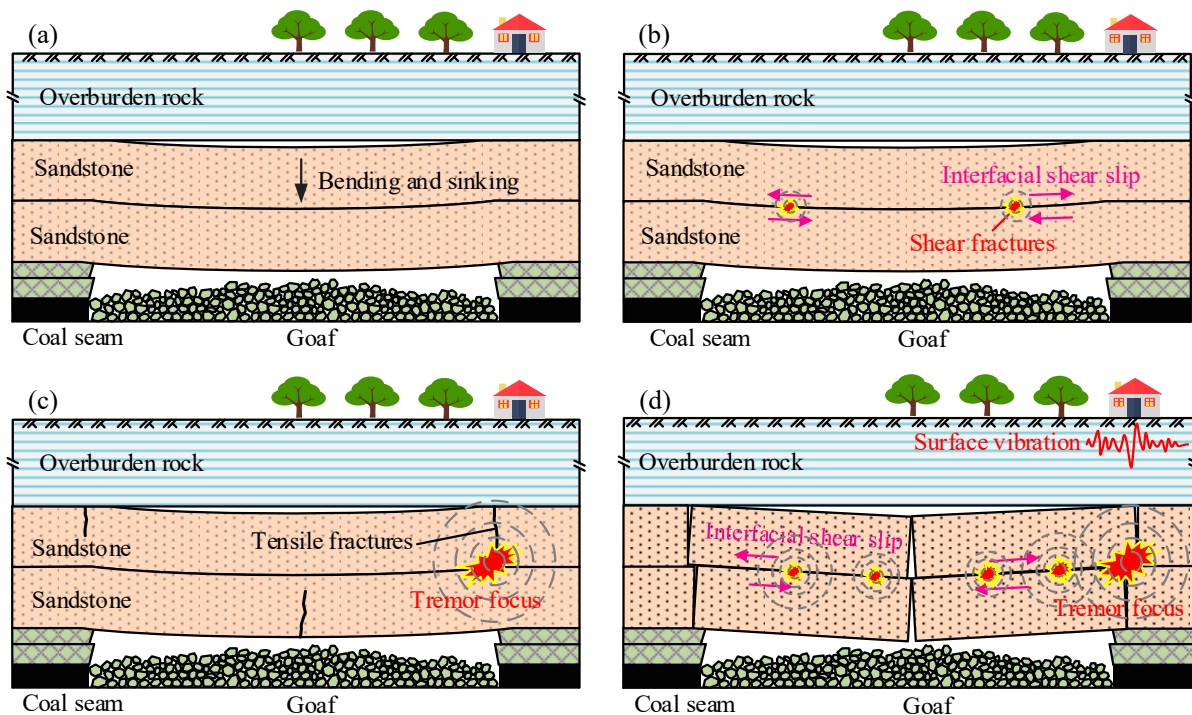


Figure 16. The process of mine tremor occurrence in a thick hard sandstone roof: (a) bending and sinking of the sandstone layers; (b) interfacial shear slips due to the bending of sandstone layers; (c) fracturing of the sandstone layers; and (d) interfacial shear slips promoted by fracturing of the sandstone layers.

When the size of the goaf reaches the limit span of the sandstone stratum, the sandstone stratum undergoes tensile fracturing (Figure 16c). The tensile fracturing releases a lot of energy and the initial tremor source appears. The development process of the tensile fractures in the sandstone stratum greatly promotes interlayer shear slippage, especially when the upper and lower layers of the sandstone fracture almost simultaneously (Figure 16d). Throughout the entire process, the interlayer shear slip occurs before the sandstone roof fractures, and it ends after the sandstone roof fractures, so the duration of the interlayer shear slip is much longer than the duration of the roof fracturing. The tensile fracturing of sandstone releases tensile waves, while the shear slip between the layers releases shear waves. Together, they constitute the seismic wave and cause the vibration of the strata and surface.

4.4. Coal Mine Tremors and Prevention Cases

Coal mine MKQ is located in the Inner Mongolia Autonomous Region, China. On 8 April 2018, a mining tremor with a magnitude of M_L 2.5 occurred on working face 3102, and the ARANMISranmis microseismic monitoring system detected an energy of 3.3×10^7 J. The tremor source was located 71 m above the coal seam, near the interface

between the 31 m-thick coarse-grained sandstone and the 28.9 m-thick medium-grained sandstone above it. The workers underground heard two consecutive heavy and dull sounds from the roof, and there was a significant vibration sensed on the surface. As shown in Figure 17, this mine tremor caused serious damage to 114 m of roadways and minor damage to 186 m of roadways. The support system was severely damaged, and production on the working face had to be stopped.

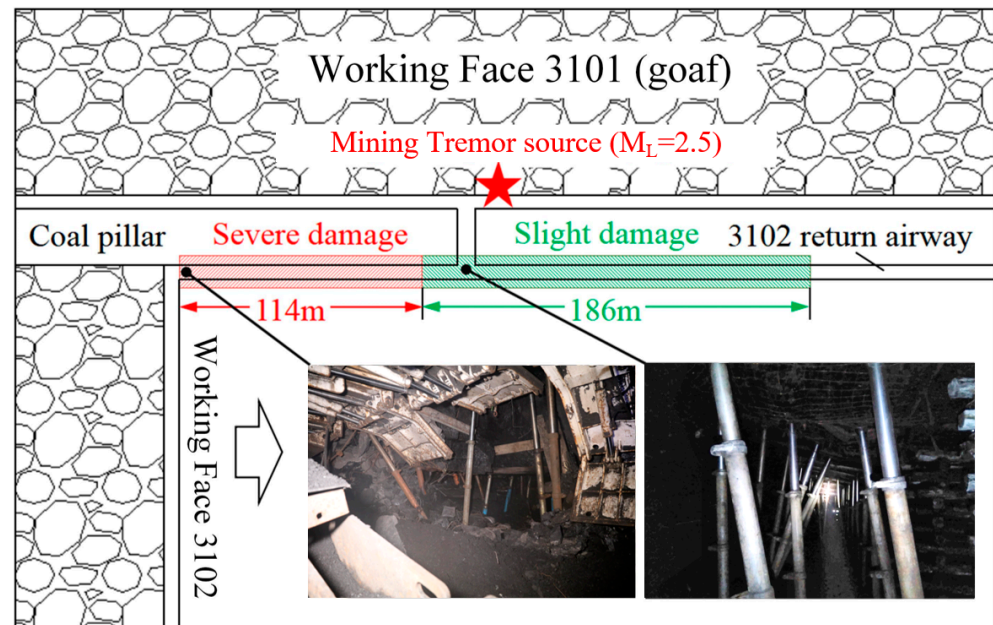


Figure 17. Location of mining tremor source and damage to a roadway.

The microseismic waveform of the tremor is shown in Figure 18. The proportion of the transverse waves of this mining tremor was higher than that of the longitudinal waves, and the duration and magnitude of the tremor were higher than those caused by the tensile fracturing of the roof of the ordinary goaf. This was the primary cause of the obvious ground shaking. The main frequency of the waveform of this mining tremor event was 0.73–7.43 Hz, with an average of 2.26 Hz. The wavelength was 498–5299 m, with an average of 3156 m. The waveform duration was 1.55–4.95 s. The source exhibited a shear–tension mixed-fracturing form dominated by shear fracturing. Thus, it is inferred that the shear fractures were likely caused by a shear slip failure between the coarse-grained sandstone and medium-grained sandstone layers.

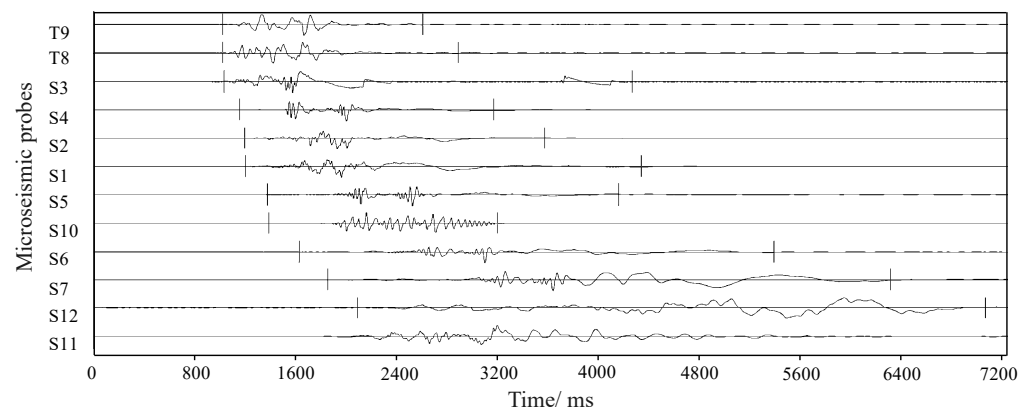


Figure 18. Waveforms of the mine tremor monitored by different seismometers.

It is clear that the closer the source of the mining tremor is to the coal seam, the more likely it is to transition from a non-hazardous mining tremor to a hazardous one. For hazardous mining tremors, preventive measures must be taken to protect the safety of the roadway. For a mining tremor involving layered rock strata, we should try to implement measures to avoid the simultaneous fracturing of the upper and lower layers of sandstone and to reduce the interlayer shear slip behaviors to reduce the energy release and duration of the mining tremor and, ultimately, reduce the damage to the underground roadway. In order to avoid mining working faces from experiencing hazardous mining tremors, for working face 3106 in the same mining area, special blasting measures were designed for the roof. The layout of the blasting holes is shown in Figure 19.

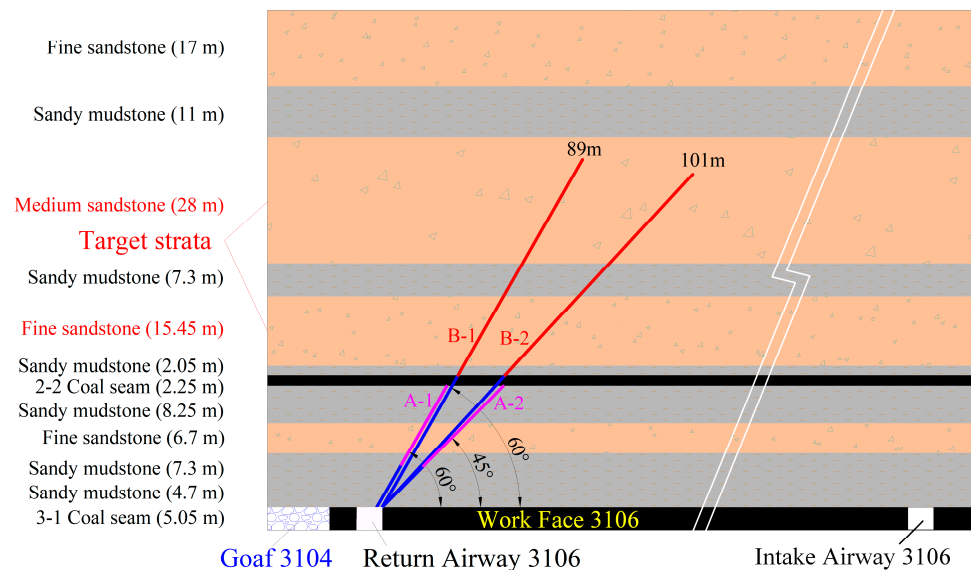


Figure 19. Borehole layout of presplitting blasting on the roof of the Return Airway 3106.

Taking coal seam 2-2 as a dividing line, the 0~115 m-thick strata above coal seam 3-1 are divided into the low-level rock strata and medium-level rock strata. For the low-level rock strata, a set of fan-shaped roof blasting holes are arranged every 20 m, including hole numbers A-1 and A-2. The angles between these holes and the coal seam are 60° and 45°, respectively, and the depths of these holes are 31 m and 38 m. The diameters of the holes are 89 mm. The purpose is to completely cut off rock strata 4 and 5 along the direction of the roadway in order to avoid the danger of coalbursts caused by the fracturing of hard stratum 4.

For the medium-level rock mass, a set of longer fan-shaped roof blasting holes are arranged every 100 m, including hole numbers B-1 and B-2. The angles between these holes and the coal seam are 60 and 47°, respectively, and the depths of these holes are 89 and 101 m. The diameters of these holes are 75 mm. The purpose is to periodically cut off hard rock strata 8 and 10 to avoid the development of large-scale hanging roofs and chains of fractures formed in rock strata 8, 10, and 12. This greatly weakens the interlayer shear slip, reducing the duration of the vibrations.

We loaded 77, 92, 224, and 226 kg of explosives, respectively, in blast holes A1, A2, B1, and B2. After the implementation of roof blasting measures, the distribution of the microseismic events with energies of greater than 10,000 J within the initial 700 m mining range of working face 3106 are shown in Figure 20. The maximum energy of the microseismic events is only 8.17×10^5 J, and no mining tremor events have occurred. This means that the treatment measures for the roof have played a certain role in preventing mine tremors. In addition, the working resistance of the fully mechanized hydraulic support in the working face increases, but the dynamic load characteristics of periodic weighting are no longer significant. In the roadway ahead of the working face, the deformation of the

roadway walls increases slightly. They indicate that part of the pressure of the roof treated by blasting is transferred to the lower coal seam, which is beneficial to the management of the goaf.

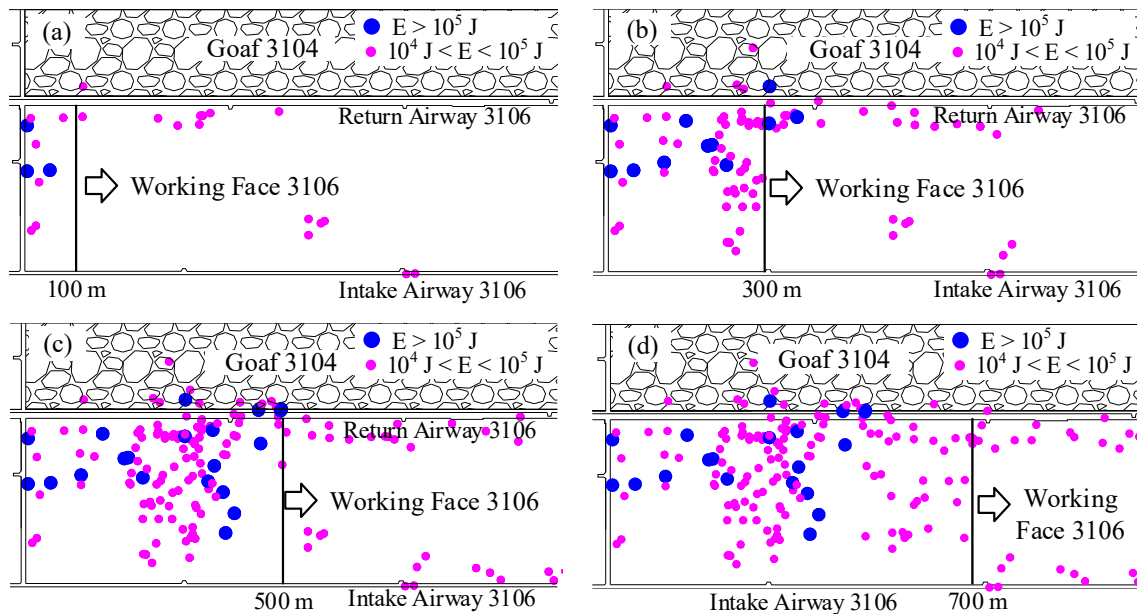


Figure 20. Distribution of microseismic events with energies of greater than 10,000 J on working face 3106 at (a) 100 m, (b) 300 m, (c) 500 m, and (d) 700 m.

In fact, the occurrence of mining tremors is sudden and difficult to effectively and accurately predict, which increases the difficulty of prevention and control. There is currently no particularly effective method for the prevention and control of roof mining tremors, especially high-level roof mining tremors. Although most mines have adopted methods for preventing and controlling coalbursts, such as ground hydraulic fracturing, separation layer grouting, roof blasting, filling mining, and increased support [31,32], new and more effective prevention and control techniques still need to be developed.

5. Conclusions

To analyze the interlayer shear slip behavior of the hard rock strata above the coal seam goaf during bending and subsidence, a three-point bending loading experiment was designed for the composite rock layers. Theoretical studies were conducted to discuss the conditions of the interlayer shear slip of the composite rock layers and the sequence of the fracturing of the upper and lower rock layers. In addition, a case study of the occurrence and prevention of coal mine tremors was conducted. The main conclusions of this study were as follows:

The interface had a significant impact on the vertical and horizontal deformations of the rock specimens. As the bending deformation increased, the difference in the horizontal deformation between the two sides of the interface continued to increase, reaching a maximum of 0.13 mm. The fracturing of the upper and lower layers of the rock promoted a transient dislocation between the layers, with dislocation amounts reaching 0.2 and 0.35 mm, and maximum shear strains of 0.025 and 0.047.

Rock bending led to an interlayer sliding deformation, while rock fracturing greatly promoted interlayer sliding. The change in the acceleration of the interlayer sliding exhibited intermittent characteristics during bending deformation, with a maximum interlayer sliding acceleration of 0.6 mm/s². During rock fracturing, the acceleration of the interlayer sliding suddenly increased, with a maximum value of 3.8 mm/s².

The acoustic emission monitoring results indicated that the interlayer shear fracturing caused the rock to undergo mixed tensile–shear fracturing rather than pure tensile fractur-

ing. During the fracture deformation stage of the rock, the proportion of shear fractures was higher than that of tensile fractures, and acoustic emission events with long durations and a high amplitude continuously occurred.

The mechanism of coal mine tremors in composite rock strata was that the increase in the area of the goaf led to the bending and subsidence of the thicker sandstone layers and interlayer shear slip. The tensile fracturing of the sandstone layer intensified the interlayer shear slip. The tensile fracturing of the sandstone released energy that generated longitudinal waves, while the interlayer shear slip released energy that generated transverse waves, causing the vibration of the roof rock strata and the surface.

Author Contributions: Conceptualization, Y.P. and X.G.; methodology, X.G.; experiment, T.Z. and W.W.; investigation, Y.X.; theoretical analysis, Y.S.; writing—original draft preparation, X.G.; writing—review and editing, Y.S.; visualization, L.D.; supervision, T.Z. All authors have read and agreed to the published version of the manuscript.

Funding: This research was funded by the National Key Research and Development Program of China (Grant No. 2022YFC3004605).

Institutional Review Board Statement: Not applicable.

Informed Consent Statement: Not applicable.

Data Availability Statement: The raw data supporting the conclusions of this article will be made available by the authors on request.

Conflicts of Interest: The authors declare no conflicts of interest.

References

1. Hasegawa, H.S.; Wetmiller, R.J.; Gendzwill, D.J. Induced seismicity in mines in Canada—An overview. *Pure Appl. Geophys.* **1989**, *129*, 423–453. [\[CrossRef\]](#)
2. Li, T.; Cai, M.F.; Cai, M. A review of mining-induced seismicity in China. *Int. J. Rock Mech. Min.* **2007**, *44*, 1149–1171. [\[CrossRef\]](#)
3. Foulger, G.R.; Wilson, M.P.; Gluyas, J.G.; Julian, B.R.; Davies, R.J. Global review of human-induced earthquakes. *Earth-Sci. Rev.* **2018**, *178*, 438–514. [\[CrossRef\]](#)
4. Alber, M.; Fritschen, R. Rock mechanical analysis of a $M_1 = 4.0$ seismic event induced by mining in the Saar District, Germany. *Geophys. J. Int.* **2011**, *186*, 359–372. [\[CrossRef\]](#)
5. Rudziński, Ł.; Cesca, S.; Lizurek, G. Complex Rupture Process of the 19 March 2013, Rudna Mine (Poland) Induced Seismic Event and Collapse in the Light of Local and Regional Moment Tensor Inversion. *Seismol. Res. Lett.* **2016**, *87*, 274–284. [\[CrossRef\]](#)
6. Alvarez-Garcia, I.N.; Ramos-Lopez, F.L.; Gonzalez-Nicieza, C.; Alvarez-Fernandez, M.I.; Alvarez-Vigil, A.E. The mine collapse at Lo Tacón (Murcia, Spain), possible cause of the Torre Pacheco earthquake (2nd May 1998, SE Spain). *Eng. Fail. Anal.* **2013**, *28*, 115–133. [\[CrossRef\]](#)
7. Ford, S.R.; Dreger, D.S.; Walter, W.R. Source Characterization of the 6 August 2007 Crandall Canyon Mine Seismic Event in Central Utah. *Seismol. Res. Lett.* **2008**, *79*, 637–644. [\[CrossRef\]](#)
8. Dong, R.S.; Xu, S.J. A Brief Discussion on Mining Earthquake Disasters—Taking the Taiji Mining Earthquake as an Example. *J. Catastrophol.* **1990**, 65–66.
9. Zhang, Y.Y.; Wang, T.T.; Su, L.N.; Yang, Y.H.; Hui, S.X. Study on the regional characteristics of the subsidence seismic records in the northern Shaanxi. *Acta Seismol. Sin.* **2020**, *42*, 684–696. [\[CrossRef\]](#)
10. He, W.Z.; Xiang, M.X.; Liu, H.N.; Li, Y.H.; Peng, J. Ground subsidence and its environment problems in Yushenfu mining area. *Coal Geol. Explor.* **2016**, *44*, 131–135. [\[CrossRef\]](#)
11. Bedford, J.D.; Faulkner, D.R.; Lapusta, N. Fault rock heterogeneity can produce fault weakness and reduce fault stability. *Nat. Commun.* **2022**, *13*, 326. [\[CrossRef\]](#) [\[PubMed\]](#)
12. Goebel, T.H.W.; Brodsky, E.E.; Dresen, G. Fault Roughness Promotes Earthquake-Like Aftershock Clustering in the Lab. *Geophys. Res. Lett.* **2023**, *50*, e2022GL101241. [\[CrossRef\]](#)
13. Chen, X.F.; Chitta, S.S.; Zu, X.M.; Reches, Z. Dynamic fault weakening during earthquakes: Rupture or friction? *Earth Planet. Sci. Lett.* **2021**, *575*, 117165. [\[CrossRef\]](#)
14. Yang, Z.Q.; Liu, C.; Zhu, H.Z.; Xie, F.X.; Dou, L.M.; Chen, J.H. Mechanism of rock burst caused by fracture of key strata during irregular working face mining and its prevention methods. *Int. J. Min. Sci. Technol.* **2019**, *29*, 889–897. [\[CrossRef\]](#)
15. Pan, C.; Xia, B.W.; Zuo, Y.J.; Yu, B.; Ou, C.N. Mechanism and control technology of strong ground pressure behaviour induced by high-position hard roofs in extra-thick coal seam mining. *Int. J. Min. Sci. Technol.* **2022**, *32*, 499–511. [\[CrossRef\]](#)
16. Wu, Q.S.; Jiang, J.Q.; Wu, Q.L.; Xue, Y.C.; Kong, P.; Gong, B. Study on the Fracture of Hard and Thick Sandstone and the Distribution Characteristics of Microseismic Activity. *Geotech. Geol. Eng.* **2018**, *36*, 3357–3373. [\[CrossRef\]](#)

17. Du, K.; Li, X.F.; Tao, M.; Wang, S.F. Experimental study on acoustic emission (AE) characteristics and crack classification during rock fracture in several basic lab tests. *Int. J. Rock Mech. Min.* **2020**, *133*, 104411. [[CrossRef](#)]
18. Zhang, W.L.; Qu, X.C.; Li, C.; Xu, X.; Zhang, S.L.; Jin, G.D.; Wang, Y.L. Fracture analysis of multi-hard roofs based on microseismic monitoring and control techniques for induced rock burst: A case study. *Arab. J. Geosci.* **2019**, *12*, 784. [[CrossRef](#)]
19. Fu, J.H.; Wen, G.G.; Sun, H.T.; Yang, X.L. Study on the shear movement law of overlying strata by slice mining. *Energy Sci. Eng.* **2020**, *8*, 2335–2351. [[CrossRef](#)]
20. Alneasan, M.; Behnia, M.; Bagherpour, R. Analytical investigations of interface crack growth between two dissimilar rock layers under compression and tension. *Eng. Geol.* **2019**, *259*, 105188. [[CrossRef](#)]
21. Li, Y.J.; Wang, S.T.; Zheng, L.G.; Zhao, S.K.; Zuo, J.P. Evaluation of the fracture mechanisms and criteria of bedding shale based on three-point bending experiment. *Eng. Fract. Mech.* **2021**, *255*, 107913. [[CrossRef](#)]
22. Wang, G.B.; Meng, T.; Feng, G.; Ma, L.F.; Yang, W.M.; He, Y.; Zhang, Z.J.; Liang, X.F. Influence of Bedding Strength and Angle on Fracture Characteristics of Sandstone under Three-Point Bending Conditions. *Appl. Sci.* **2023**, *13*, 8216. [[CrossRef](#)]
23. Zhen, X.X.; Zang, Z.J.; Wang, R.H.; Li, Z. Influence of slip effect on bending characteristics offrictional laminated beams. *Eng. Mech.* **2016**, *33*, 185–193. [[CrossRef](#)]
24. Shabanimashcool, M.; Li, C.C. Analytical approaches for studying the stability of laminated roof strata. *Int. J. Rock Mech. Min.* **2015**, *79*, 99–108. [[CrossRef](#)]
25. Sterling, R.L. The Ultimate Load Behavior of Laterally Constrained Rock Beams. In Proceedings of the 21st U.S. Symposium on Rock Mechanics, Rolla, MO, USA, 28–30 May 1980; pp. 80–533.
26. Chang, X.; Shan, Y.F.; Zhang, Z.H.; Tang, C.A.; Ru, Z.L. Behavior of propagating fracture at bedding interface in layered rocks. *Eng. Geol.* **2015**, *197*, 33–41. [[CrossRef](#)]
27. Xiao, Y. Interlaminar shear slip condition of stratified rock mass under bending. In Proceedings of the Second National Engineering Geomechanics Youth Symposium, Beijing, China, 1 March 1992.
28. Skrzypkowski, K.; Zagórski, K.; Zagórska, A. Determination of the Extent of the Rock Destruction Zones around a Gasification Channel on the Basis of Strength Tests of Sandstone and Claystone Samples Heated at High Temperatures up to 1200 °C and Exposed to Water. *Energies* **2021**, *14*, 6464. [[CrossRef](#)]
29. Aldahdooh, M.A.A.; Muhamad Bunnori, N. Crack classification in reinforced concrete beams with varying thicknesses by mean of acoustic emission signal features. *Constr. Build. Mater.* **2013**, *45*, 282–288. [[CrossRef](#)]
30. Wang, W.; Zhao, Y.X.; Gao, Y.R.; Zhang, C. Experimental research of influences of bedding and pre-crack directions on fracture characteristics of coal. *Chin. J. Rock Mech. Eng.* **2022**, *41*, 433–445. [[CrossRef](#)]
31. Wang, W.; Pan, Y.S.; Xiao, Y.H. Synergistic resin anchoring technology of rebar bolts in coal mine roadways. *Int. J. Rock Mech. Min. Sci.* **2022**, *151*, 105034. [[CrossRef](#)]
32. Wang, W.; Pan, Y.S.; Xiao, Y.H. Synergistic mechanism and technology of cable bolt resin anchoring for roadway roofs with weak interlayers. *Rock Mech. Rock Eng.* **2022**, *55*, 3451–3472. [[CrossRef](#)]

Disclaimer/Publisher’s Note: The statements, opinions and data contained in all publications are solely those of the individual author(s) and contributor(s) and not of MDPI and/or the editor(s). MDPI and/or the editor(s) disclaim responsibility for any injury to people or property resulting from any ideas, methods, instructions or products referred to in the content.